Multi-wavelength study of triggered star formation around 25 H II regions [*]

Jin-Long Xu[1,2], Jun-Jie Wang[1,2], Chang-Chun Ning[2,3] and Chuan-Peng Zhang[1,2,4]

[1] National Astronomical Observatories, Chinese Academy of Sciences, Beijing 100012, China
xujl@bao.ac.cn
[2] NAOC-TU Joint Center for Astrophysics, Lhasa 850000, China
[3] Tibet University, Lhasa 850000, China
[4] University of Chinese Academy of Sciences, Beijing 100049, China

Abstract We investigate 25 H II regions that show bubble morphology in ^{13}CO(1–0) and infrared data, to search for quantitative evidence of triggered star formation by processes described by the collect and collapse (CC) and radiatively driven implosion (RDI) models. These H II regions display the morphology of a complete or partial bubble at 8 μm, and are all associated with the molecular clouds that surround them. We found that the electron temperature ranges from 5627 K to 6839 K in these H II regions, and the average electron temperature is 6083 K. The age of these H II regions is from 3.0×10^5 yr to 1.7×10^6 yr, and the mean age is 7.7×10^5 yr. Based on the morphology of the associated molecular clouds, we divide these H II regions into three groups, which may support CC and RDI models. We select 23 young IRAS sources which have an infrared luminosity of $>10^3 L_\odot$ in 19 H II regions. In addition, we identify some young stellar objects (including Class I sources), which are only concentrated in H II regions G29.007+0.076, G44.339–0.827 and G47.028+0.232. The polycyclic aromatic hydrocarbon emissions of the three H II regions all show a cometary globule. Comparing the age of each H II region with the characteristic timescales for star formation, we suggest that the three H II regions can trigger clustered star formation by an RDI process. In addition, we detect seven molecular outflows in the five H II regions for the first time. These outflow sources may be triggered by the corresponding H II regions.

Key words: H II regions — ISM: bubbles — stars: formation — stars: protostars

1 INTRODUCTION

Isolated low-mass star formation is well understood, but the scenario describing massive star formation and clustered star formation remains unclear. The feedback of a massive star has a significant impact on its surrounding environment, such as an H II region, stellar winds and a supernova remnant (SNR) (Zinnecker & Yorke 2007; Dewangan et al. 2012).

On one hand, when these energetic products of a massive star propagate into the surrounding molecular clouds, they cause overdensities along the advancing boundary and some dense cores form. On the other hand, when these energetic products of a massive star collide with some pre-existing compact cloud cores, they trigger the cloud cores to collapse. The triggered stars may form more quickly than quiescent isolated stars. Moreover, an H II region, stellar winds and an SNR may impact a large range of molecular clouds, triggering clustered star formation.

Previous observations toward some SNRs (Junkes et al. 1992; Paron et al. 2009; Xu et al. 2011; Xu & Wang 2012) have suggested that although some young stars are distributed around the SNRs, the age that was obtained for these SNRs is not greater than the time scales required for young stars. What did trigger these young stars? SNRs and/or stellar winds of their progenitors may move through the molecular shell produced by an H II region (Junkes et al. 1992; Paron et al. 2009; Su et al. 2009; Zhou et al. 2009), so the young stars found surrounding the SNR may explode in the molecular shell produced by an HII region and/or stellar winds.

Previous studies on individual H II regions suggest that H II regions can trigger formation of young stars (for example, Zavagno et al. 2010; Dewangan et al. 2012; Paron et al. 2011; Dirienzo et al. 2012). Two processes have been considered to explain the process of triggered star formation at the edge of H II regions, namely collect and collapse (CC) (Dale et al. 2007) and radiation driven implosion (RDI) (Sandford et al. 1982). In the CC process, a compressed layer of neutral, high-density material forms between the ionization front and shock front preceding it in the neutral gas, and star formation occurs when this layer becomes gravitationally unstable. This model was first proposed by Elmegreen & Lada (1997). Massive star formation may be triggered by a CC process (Whitworth et al. 1994). In an RDI process, the shocks drive into dense, pre-existing structures and compress them to form stars, which are characterized by cometary globules or optically bright rims. Bright-rimmed clouds (BRCs) found in H II regions are sites that potentially show triggered star formation from the RDI process. The RDI process may trigger formation of low-mass and intermediate-mass stars (Reipurth 1983).

Recently, observational searches for evidence of triggered star formation focused on bubbles described by Churchwell et al. (2006). Churchwell et al. (2006) concluded that about 25% of the bubbles coincide with known radio H II regions, while Deharveng et al. (2010) suggested that about 86% of the bubbles contain ionized gas detected by the radio-continuum emission. Although nearly all GLIMPSE bubbles may be caused by H II regions, about half of all Galactic H II regions have a bubble morphology in the infrared band (Bania et al. 2010).

In this paper, we study 25 H II regions with bubble-like morphologies in a consistent way to analyze triggered star formation in H II regions. In Section 2, we summarize characteristics of the selected sample of H II regions and young stars. In Section 3, we give the general results and discussion. In Section 4, we summarize our main conclusions.

2 DATA

2.1 Sample Selection

The target sample was constructed by applying the following criteria. (1) The selected H II regions are in overlapping regions observed by the GBT, Arecibo, GRS, NVSS and GLIMPSE surveys. (2) The size of each selected H II region must be greater than the beam size of the surveys. (3) The selected H II regions have a bubble morphology at 8 μm. From these criteria, we selected 25 H II regions as our sample, 16 of which are associated with Churchwell et al. (2006) bubbles.

Table 1 lists the names and parameters describing the sample of targets including the Galactic longitude and latitude, local standard of rest (LSR) velocity of Hα and integrated flux density (S). A description of these surveys is given below.

In the GBT survey (Anderson et al. 2011), 448 previously unknown Galactic H II regions were detected at the X-band (9 GHz, 3 cm) in the Galactic zone $343° \leq l \leq 67°$ and $|b| \leq 1°$. The FWHM

Table 1 H II Region Sample and CO Parameters

No.	Region	l (°)	b (°)	T_{mb} (K)	FWHM (km s^{-1})	V_{LSR} (km s^{-1})	$V_{H\alpha}$ (km s^{-1})	S (mJy)	D (kpc)	R (pc)	N_{H_2} (cm^{-2})	n_i (10^{3}cm^{-3})	
1	G19.504−0.193	19.504	−0.193	2.6	9.4(0.4)	38.9(0.2)	37.8	168	12.8^a	2.8	1.5×10^{22}	3.5	N25
2	G19.813+0.010	19.813	+0.010	2.3	4.4(0.2)	57.5(0.1)	60.4	187	11.8^b	5.8	6.3×10^{21}	1.7	N27
3	G23.029−0.405	23.029	−0.405	7.4	7.7(0.2)	74.6(0.1)	76.0	1014	4.7^a	3.6	3.6×10^{22}	3.2	
4	G26.824+0.380	26.824	+0.380	2.6	2.4(0.1)	80.9(0.1)	82.0	120	4.9^a	2.2	3.9×10^{21}	1.5	N44
5	G29.007+0.076	29.007	+0.076	2.8	4.8(0.6)	70.3(0.2)	67.7	454	11.5^a	7.1	8.4×10^{21}	1.2	N50
6	G32.587+0.006	32.587	+0.006	2.4	8.4(0.4)	74.5(0.2)	77.4	273	9.7^a	4.3	1.3×10^{22}	4.1	N56
7	G32.976−0.334	32.976	−0.334	4.5	4.4(0.1)	49.8(0.1)	49.3	492	11.0^a	7.3	1.2×10^{22}	2.5	
8	G33.718−0.410	33.718	−0.410	1.8	3.9(0.2)	49.9(0.1)	53.3	151	3.3^a	1.4	4.4×10^{21}	2.7	
9	G34.325+0.211	34.325	+0.211	3.9	4.0(0.4)	56.9(0.1)	62.9	307	10.3^a	5.9	9.8×10^{21}	1.2	N62
10	G38.353−0.134	38.353	−0.134	1.2	4.0(0.5)	70.3(0.2)	70.5	93.0^d	8.6^b	3.2	3.0×10^{21}	0.5	N72
11	G38.643−0.227	38.643	−0.227	2.6	5.1(0.3)	67.9(0.3)	63.8	86	8.7^a	3.1	8.3×10^{21}	2.4	
12	G38.738−0.140	38.738	−0.140	4.1	2.0(0.1)	64.9(0.1)	60.9	213	8.9^a	3.2	5.1×10^{21}	1.1	N73
13	G38.930−0.386	38.930	−0.386	6.6	3.9(0.1)	39.7(0.1)	42.1	38	2.7^a	0.7	1.6×10^{22}	6.2	N75
14	G41.132−0.558	41.132	−0.558	2.5	3.8(0.4)	62.4(0.1)	65.5	14.2^d	6.4^c	2.5	5.9×10^{21}	1.7	
15	G41.239−0.176	41.239	−0.176	6.1	10.0(0.3)	59.0(0.5)	56.9	440	8.7^a	3.8	3.8×10^{22}	9.0	
16	G41.928+0.029	41.928	+0.029	1.6	4.0(0.4)	17.7(0.2)	20.7	620	11.4^a	5.7	4.0×10^{21}	0.8	N80
17	G43.738+0.114	43.738	+0.114	1.8	1.6(0.3)	71.0(0.1)	73.1	15.4^d	6.1^c	4.2	2.3×10^{21}	0.6	N89
18	G43.770+0.070	43.770	+0.070	1.2	2.1(0.2)	68.7(0.1)	70.5	360	6.1^a	3.8	2.3×10^{21}	1.2	N90
19	G44.339−0.827	44.339	−0.827	4.0	3.3(0.1)	61.7(0.1)	62.5	136	6.1^a	4.1	8.3×10^{21}	1.7	N92
20	G45.770−0.372	45.770	−0.372	1.8	10.0(0.2)	58.0(0.1)	51.0	15.0^d	5.8^b	2.2	1.1×10^{22}	0.8	
21	G46.176+0.536	46.176	+0.536	2.1	3.0(0.2)	13.0(0.1)	6.3	30.0^d	10.8^c	2.5	3.9×10^{21}	0.9	
22	G47.028+0.232	47.028	+0.232	4.3	3.7(0.1)	56.4(0.1)	56.9	390	5.8^a	3.8	1.0×10^{22}	1.6	N98
23	G49.738−0.616	49.738	−0.616	3.0	2.2(0.1)	67.8(0.1)	62.4	37.3^d	5.5^c	3.8	4.1×10^{21}	0.8	
24	G50.039−0.274	50.039	−0.274	4.1	2.0(0.2)	62.5(0.1)	60.9	—	5.5^c	2.9	5.1×10^{21}	1.9	N104
25	G50.079+0.571	50.079	+0.571	2.1	3.3(0.1)	−2.0(0.1)	−1.1	195	11.1^a	3.8	4.1×10^{21}	0.5	N105

Notes: ^{a}Distances are determined with the H I E/A and ^{13}CO(1–0) methods. ^{b}Distances are only based on the judgement of ^{13}CO(1–0) with regard to the kinematic distance ambiguity. ^{c}Distances are obtained from the judgement of Bania et al. (2012) with regard to the kinematic distance ambiguity. ^{d}The integrated flux at 1.4 GHz.

beam size of the telescope was approximately 82″ at this frequency. Additionally, in the Arecibo survey of H II regions, Bania et al. (2012) reported the discovery of 37 previously unknown H II regions at the X-band (9 GHz, 3 cm). The survey covered the Galactic zone of $31° \leq l \leq 66°$ with $|b| \leq 1°$. Its beam was nearly three times smaller than that of the GBT.

To trace the ionized gas and investigate the distribution of molecular gas in the surrounding H II regions, we used the NVSS and BU-FCRAO GRS surveys. NVSS is a 1.4 GHz continuum survey covering the entire sky north of the declination –40° (Condon et al. 1998) with a noise of about 0.45 mJy/beam and a resolution of 45″, while the BU-FCRAO GRS is a new survey of Galactic ^{13}CO(1–0) emission (Jackson et al. 2006). The survey covers a Galactic longitude range of $l = 18°$–55.7° and a Galactic latitude range of $|b| \leq 1°$, with an angular resolution of 46″. The survey's velocity coverage is –5 to 135 km s^{-1} for Galactic longitudes $l \leq 40°$ and –5 to 85 km s^{-1} for Galactic longitudes $l > 40°$. At the velocity resolution of 0.21 km s^{-1}, the typical root mean square sensitivity is 0.13 K.

The GLIMPSE survey is used to identify the young stars along H II regions, which are observed in the Galactic plane ($65° < |l| < 10°$ for $|b| < 1°$) with the four mid-IR bands (3.6, 4.5, 5.8 and 8.0 μm) of the Infrared Array Camera (IRAC) (Fazio et al. 2004) on the Spitzer Space Telescope. The resolution ranges from 1.5″ (3.6 μm) to 1.9″ (8.0 μm).
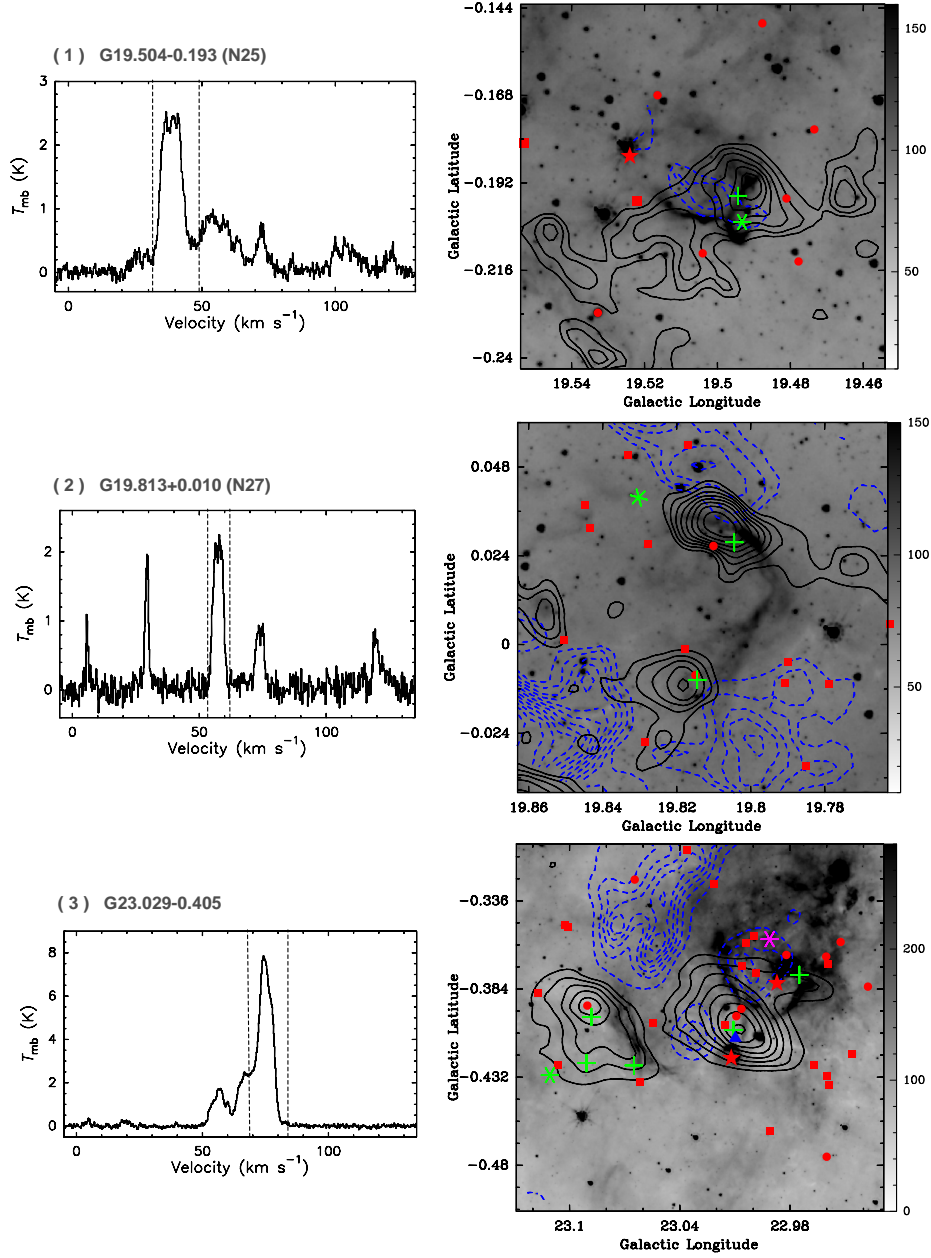
Fig. 1 *Left panels*: ^{13}CO $J = 1 - 0$ spectral profile averaged over the molecular clouds. Two black dashed lines mark the integrated velocity ranges and tangent point velocity, respectively. *Right panels*: ^{13}CO $J = 1 - 0$ integrated intensity (*black contours*) and 1.4 GHz continuum emission (*blue dashed contours*) maps are overlayed on the mid-infrared 8 μm emission map (gray scale). The blue contour levels begin at the peak flux of 20% and increase in steps of 10% of the peak flux. Class I sources are labeled as red circles, and Class II sources as red squares. The red stars represent IRAS sources. The green pluses and green asterisks indicate the millmeter continuum sources and X ray sources, respectively. The pink asterisk marks the SNR candidate. The contour levels are (1) 10.0, 10.7, 11.4, 12.1, 12.8, 13.6 and 14.3 km s^{-1}. (2) 2.9, 3.4, 3.8, 4.3, 4.7, 5.2, 5.6 and 6.1 km s^{-1}. (3) 19.3, 22.0, 24.5, 27.5, 30.2, 32.9, 35.6 and 38.3 km s^{-1}.

(4) G26.824+0.380
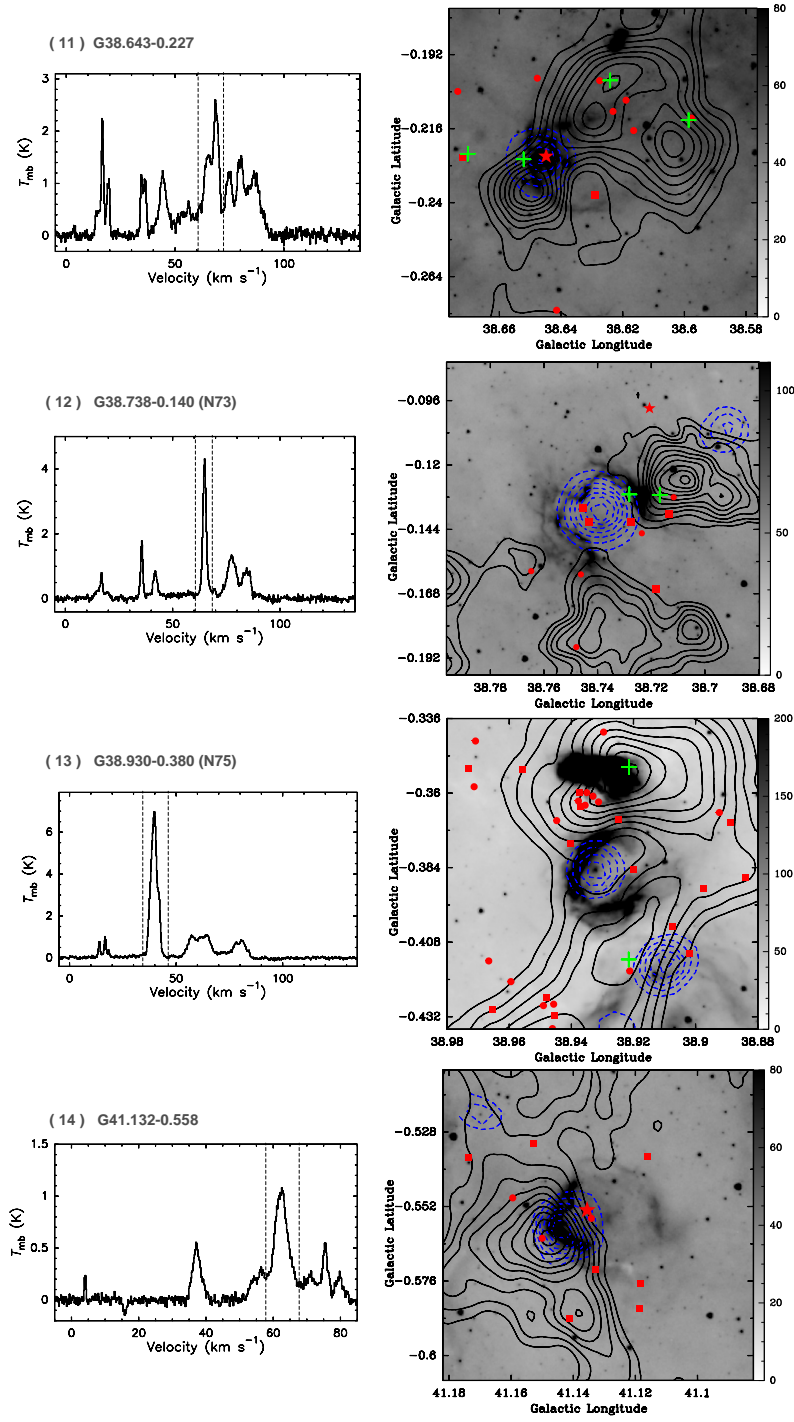

(5) G29.007+0.076 (N50)

(6) G32.587+0.006 (N56)
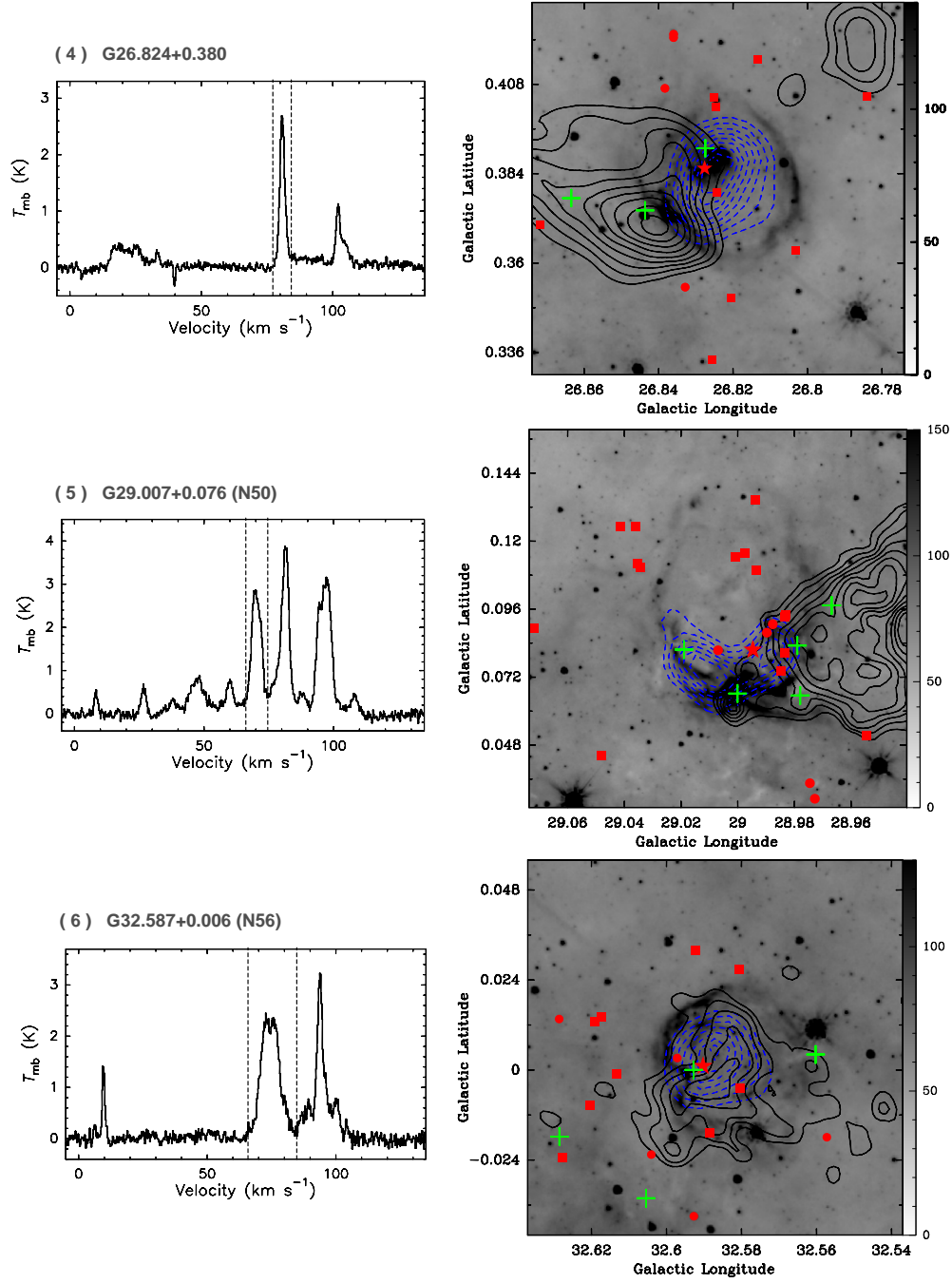
Fig. 1 *Continued.* The contour levels are (4) 2.0, 2.4, 2.7, 3.1, 3.5, 3.8, 4.2, 4.5 and 4.9 km s^{-1}. (5) 3.5, 4.0, 4.7, 5.4, 6.0, 6.7, 7.4 and 8.0 km s^{-1}. (6) 5.2, 6.3, 7.3, 8.3, 9.4, 10.4, 12.5, 13.6 and 14.6 km s^{-1}.
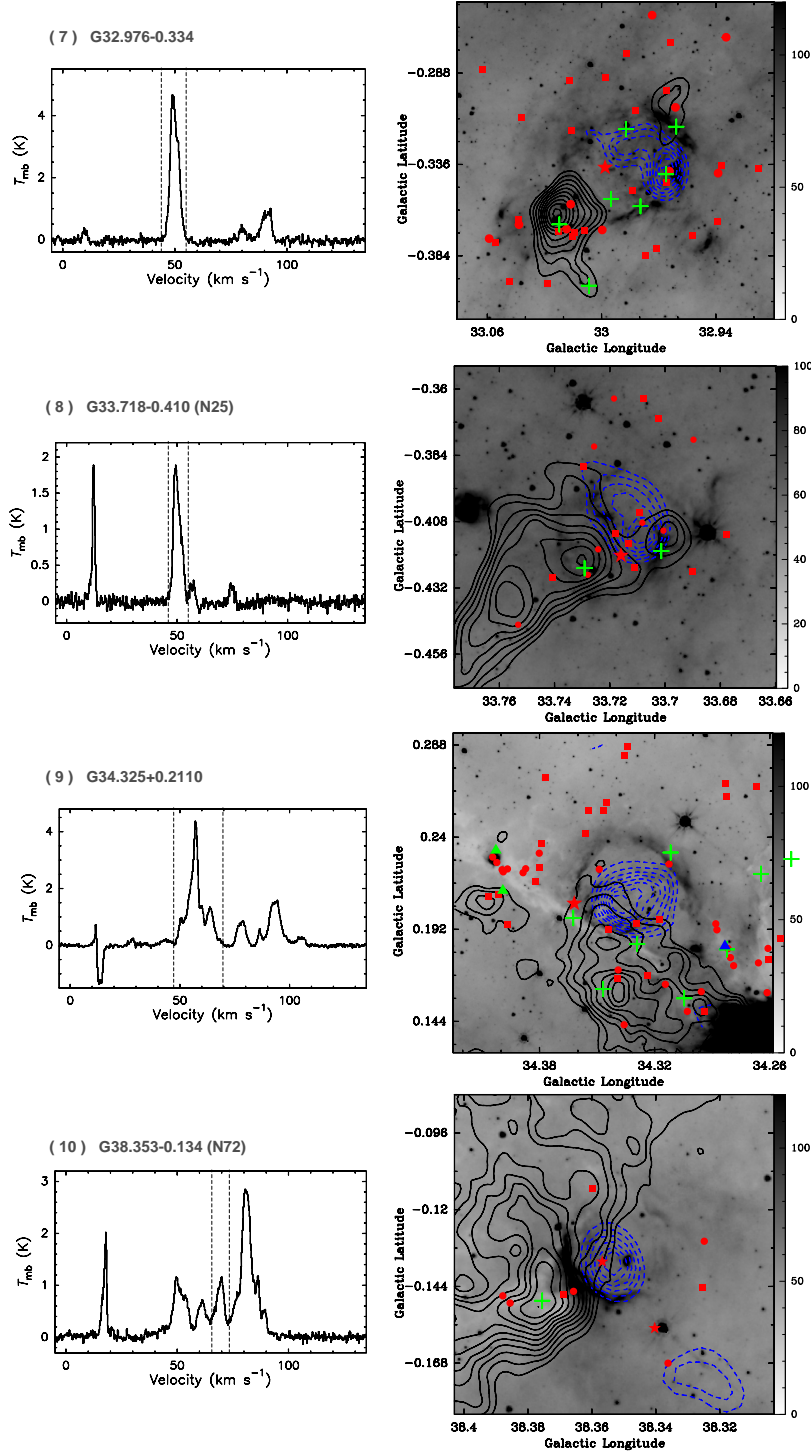
Fig. 1 *Continued.* The contour levels are (7) 5.2, 6.3, 7.3, 8.3, 9.4, 11.5, 12.5, 13.6 and 14.6 km s^{-1}. (8) 2.5, 2.8, 3.1, 3.5, 3.8, 4.2, 4.5 and 4.8 km s^{-1}. (9) 3.7, 4.3, 4.8, 5.4, 6.0, 6.5, 7.1 and 7.7 km s^{-1}. (10) 5.9, 6.5, 7.1, 7.7, 8.3, 8.9, 9.5, 10.1, 10.7, 11.3 and 11.8 km s^{-1}.

Fig. 1 *Continued.* The contour levels are (11) 5.3, 6.1, 6.9, 7.7, 8.5, 9.3, 10.2 and 11.0 km s^{-1}. (12) 2.7, 3.3, 3.8, 4.3, 4.9, 5.4, 6.0, 6.5, 7.0 and 7.6 km s^{-1}. (13) 7.6, 9.1, 10.7, 12.2, 13.7, 15.2, 16.7, 18.3, 19.8 and 21.3 km s^{-1}. (14) 2.7, 3.2, 3.8, 4.3, 4.9, 5.4, 5.9, 6.5, 7.0, and 7.5 km s^{-1}.

(15) G41.239-0.176

(16) G41.928+0.029 (N80)

(17+18) G43.738 (N89), G43.770 (N90)

(19) G44.339-0.827 (N92)
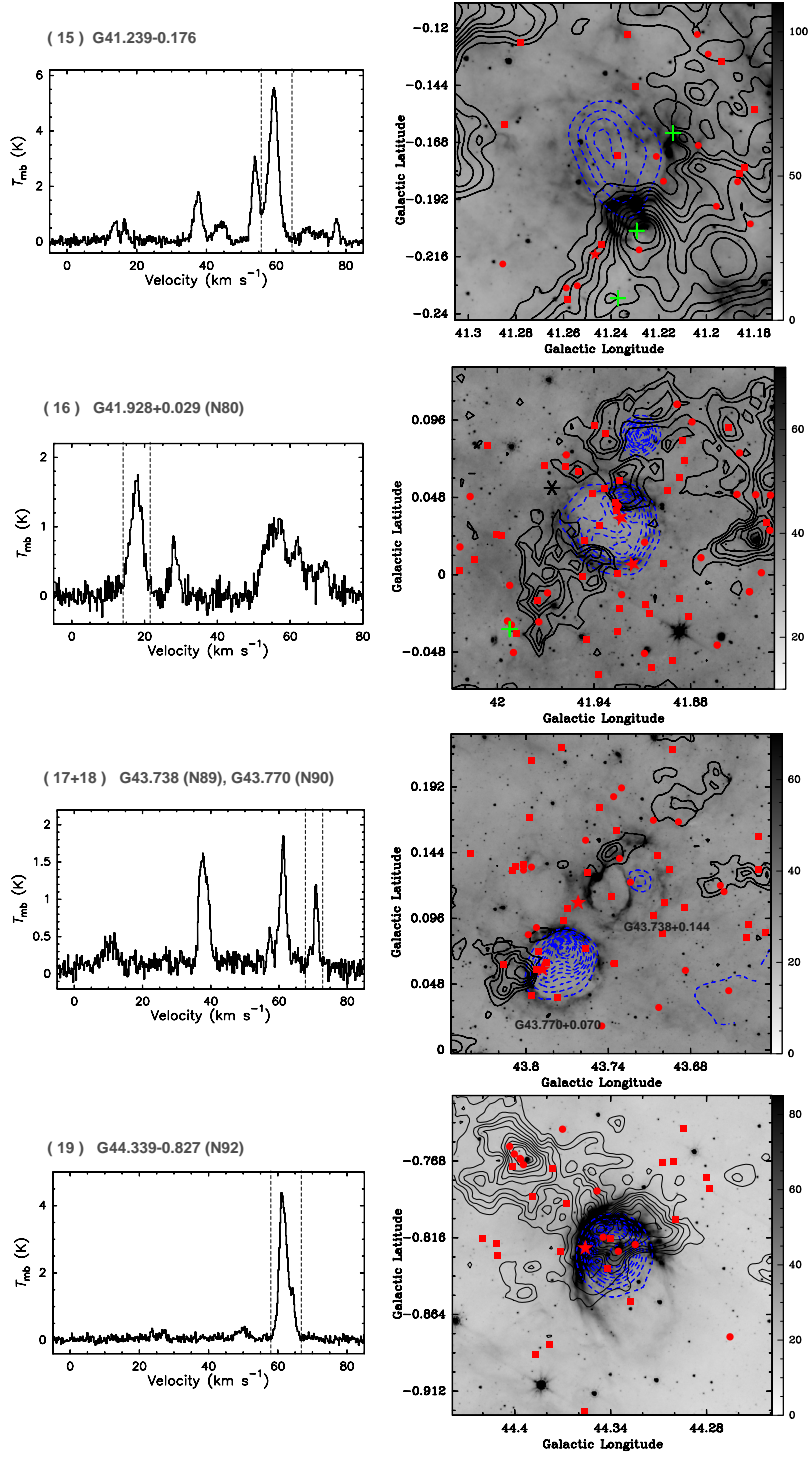
Fig. 1 *Continued.* The contour levels are (15) 4.2, 5.2, 6.2, 7.2, 8.2, 9.2, 10.2 and 11.2 km s^{-1}. (16) 2.3, 3.0, 3.6, 4.3, 4.9, 5.6, 6.2, 6.9, 7.5, 8.2 and 8.8 km s^{-1}. (17+18) 0.9, 1.3, 1.8, 2.2 and 2.7 km s^{-1}. (19) 4.6, 5.3, 5.9, 6.6, 7.3, 8.0, 8.7, 9.4, 10.1, 10.7 and 11 km s^{-1}.

(20) G45.770-0.372

(21) G46.176+0.536

(22) G47.028+0.232 (N98)

(23) G49.738-0.616
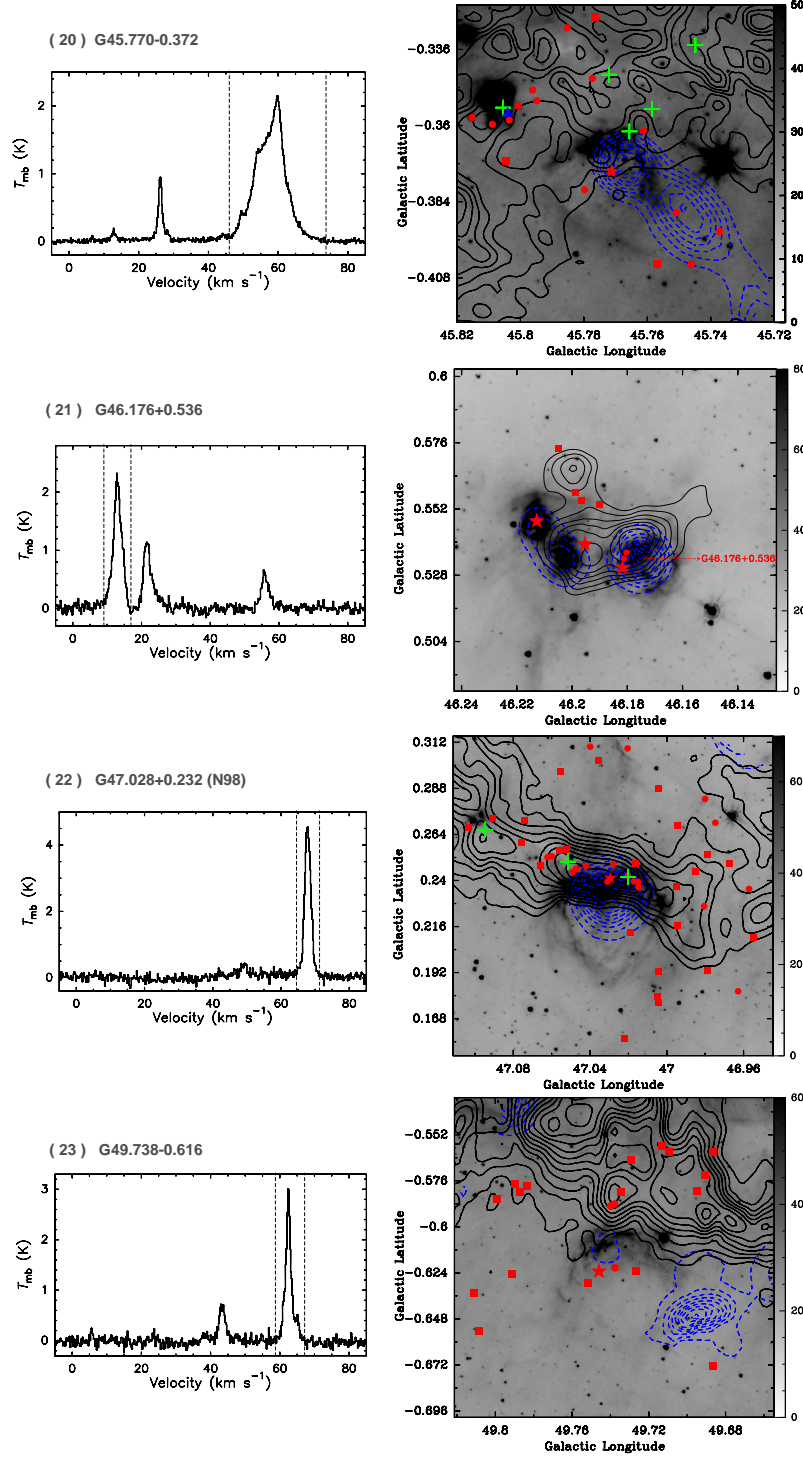
Fig. 1 *Continued.* The contour levels are (20) 7.8, 8.8, 9.7, 10.6, 11.6, 12.5, 13.4, 14.4 and 15.3 km s^{-1}. (21) 1.6, 2.1, 2.6, 3.2, 3.7, 4.2, 4.7 and 5.3 km s^{-1}. (21) 4.7, 5.9, 7.1, 8.4, 9.6, 10.9, 11.1, 13.3 and 14.6 km s^{-1}. (23) 0.8, 1.4, 2.0, 2.6, 3.2, 3.8, 4.4, 5.0, 5.6, 6.2, 6.8 and 7.4 km s^{-1}.
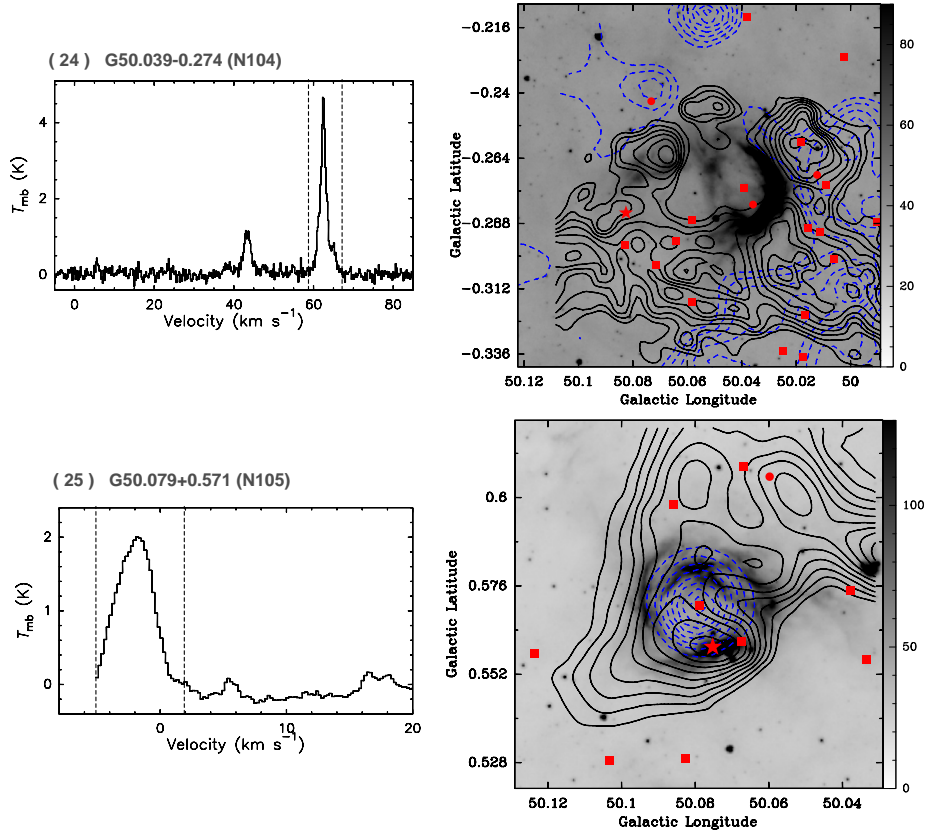
Fig. 1 *Continued.* The contour levels are (24) 2.9, 3.4, 3.9, 4.4, 4.9, 5.5, 6.0, 6.5 and 7.0 km s^{-1}. (25) 4.1, 4.9, 5.6, 6.3, 7.0, 7.8, 8.5, 9.2 and 9.9 km s^{-1}.

3 RESULTS AND DISCUSSION

3.1 H II Regions

3.1.1 *The morphology of* H II *regions*

Figure 1 (right panels) shows contours of the 1.4 GHz continuum emission (blue) superimposed on the Spitzer-IRAC 8 μm image of each H II region (color scale). The 8 μm IRAC band contains emission from polycyclic aromatic hydrocarbons (PAHs). PAHs are believed to be destroyed in the ionized gas, but thought to be excited at the interface of the H II region and molecular cloud by radiation leaking from the H II region. Hence, triggered formation of young stars can easily be found in the molecular clouds adjacent to the 8 μm emission. In Figure 1 (right panels), the 8 μm emission displays the morphology of complete or partial bubbles. The 1.4 GHz continuum emission reveals the presence of ionized gas in each H II region. From Figure 1 (right panels), we can see that the 8 μm bubble of these H II regions are filled with the 1.4 GHz continuum emission (blue contours), except for G19.813+0.010 and G50.039–0.274. The blue contours are not found in the centers of G19.813+0.010 and G50.039–0.274. Hence, PAH emission may be excited by the radiation leaking from these H II regions. In the G41.928+0.029 region, there may be another H II region located to the

northwest, which is surrounded by the shell-like molecular gas. Through the morphology exhibited by 8 μm emission, we can measure the sizes of each bubble, which are listed in Table 1.

3.1.2 *The distance to* H II *regions*

CO data are widely used to trace the morphology of molecular clouds. The average ^{13}CO(1–0) spectrum in each H II region is presented in Figure 1 (left panels). From these panels, we can see that spectra of 25 H II regions show multiple velocity components detected along the line of sight, except for H II regions G44.339–0.827, G47.028+0.232 and G49.738–0.616. According to the hydrogen radio recombination line velocity components of each H II region given by Anderson et al. (2011), we select the velocity components of ^{13}CO(1–0) associated with the H II regions, whose peak is located between two vertical dashed lines in Figure 1 (left panels). Through Gaussian fits to all the spectra, we obtain the central line velocity (V_{LSR}), the peak intensity (T_{mb}) and full width at half maximum (FWHM).

Based on the Galactic rotation model of Fich et al. (1989) together with $R_{\odot} = 8.5\,$kpc and $V_{\odot} = 220\,$km s^{-1}, where $V_{\odot}$ is the circular rotation speed of the Galaxy, we derive the kinematic distances of these H II regions. However, an H II region at a specific radial velocity can be at either a near or far kinematic distance, resulting in an ambiguity in the distance. The H I self-absorption features are produced when cool H I clouds absorb the warmer H I emission from the continuum emission of the background H II region. H I emission/absorption (H I E/A) is considered to be an effective method to resolve the distance ambiguity (Kuchar & Bania 1994; Kolpak et al. 2003; Anderson et al. 2011). Anderson et al. (2011) and Bania et al. (2012) have resolved the ambiguity in kinematic distance in 22 of our selected H II regions with this method. Because it is difficult to identify the H I absorption associated with the H II region above error estimates, they did not give the distances of the other four H II regions. For the H I E/A method, whether or not every line of sight between the near and far distance contains cool H I clouds is important. The cool H I clouds are also traced by optically thin ^{13}CO(1–0), whose emission is relatively stronger. H I E/A, with the addition of ^{13}CO(1–0), may accurately resolve the ambiguity in kinematic distance. If ^{13}CO(1–0) emission that coincides with H I absorption is detected between the H II region velocity and the tangent-point velocity, it suggests the H II region is at the far distance. On the contrary, it is at the near distance. Using the H I E/A and ^{13}CO(1–0) method, we check the distance of 13 H II regions from the GBT survey of H II regions, and give the distances of G26.824+0.380, G33.718–0.410, G38.930–0.386 and G41.239+0.029. Because Bania et al. (2012) did not give the H I absorption spectrum of seven H II regions from the Arecibo survey of H II regions, we did not adopt their judgement about the kinematic distance ambiguity. In addition, we also cannot provide a judgement about another three H II regions, G19.813+0.010, G38.353–0.134 and G45.770–0.372. In 23 of 25 selected H II regions, 12 are at the far distance, eight are at the tangent-point distance and three are at the near distance.

In Figure 1 (left panels), we find that if an H II region is at the far distance, the ^{13}CO(1–0) spectrum of the associated molecular clouds has several velocity components between the tangent-point and system velocity. Because G19.813+0.010 and G38.353–0.134 have several velocity components between the tangent-point and system velocity, we suggest that both H II regions may be at the far distance. If the velocity of G45.770–0.372 is near the tangent-point velocity, we adopt the tangent-point distance as that of G45.770–0.372. The fitted and obtained results are summarized in Table 1.

3.1.3 *The age of* H II *regions*

The above analysis suggests that the characteristics of the surrounding medium may affect the processes of triggered star formation. Moreover, the time scale is also important for deciding if triggered star formation is occurring. Assuming each H II region is expanding into a homogeneous medium, the dynamical ages of each H II region can be estimated by using the model (Dyson & Williams

1980)

$$t_{\mathrm{HII}} = 7.2 \times 10^4 \left(\frac{R_{\mathrm{HII}}}{\mathrm{pc}}\right)^{4/3} \left(\frac{Q_{\mathrm{Ly}}}{10^{49}\ \mathrm{s}^{-1}}\right)^{-1/4} \left(\frac{n_{\mathrm{i}}}{10^3\ \mathrm{cm}^{-3}}\right)^{-1/2}\ \mathrm{yr}, \tag{1}$$

where R_{HII} is the radius of the H II region, n_{i} is the initial number density of the gas and Q_{Ly} is the ionizing luminosity. Because the 8 μm bubbles of these H II regions are filled with the 1.4 GHz continuum emission, we take the size of the bubbles as the radius of the H II regions. In previous studies toward several H II regions (Zavagno et al. 2006; Deharveng et al. 2008; Paron et al. 2009, 2011; Pomarès et al. 2009; Dirienzo et al. 2012), they all determined an initial number density of $\sim 10^3$ cm^{-3}. Here, we also adopt an initial number density of $\sim 10^3$ cm^{-3} for all the H II regions. Assuming the emission is optically thin free-free thermal continuum, Q_{Ly} was computed by Mezger et al. (1974)

$$Q_{\mathrm{Ly}} = 4.761 \times 10^{48} a(\nu, T_{\mathrm{e}})^{-1} \left(\frac{\nu}{\mathrm{GHz}}\right)^{0.1} \left(\frac{T_{\mathrm{e}}}{\mathrm{K}}\right)^{-0.45} \left(\frac{S_\nu}{\mathrm{Jy}}\right) \times \left(\frac{D}{\mathrm{kpc}}\right)^2\ \mathrm{photon\ s}^{-1}, \tag{2}$$

where ν is the frequency of the observation, S_ν is the observed specific flux density and D is the distance to the H II region. $a(\nu, T_{\mathrm{e}})$ is defined by Mezger & Henderson (1967)

$$a(\nu, T_{\mathrm{e}}) = 0.366 \left(\frac{T_{\mathrm{e}}}{\mathrm{K}}\right)^{-0.15} \left(\frac{\nu}{\mathrm{GHz}}\right)^{0.1} \left\{\ln\left[4.995 \times 10^{-2} \times \left(\frac{\nu}{\mathrm{GHz}}\right)^{-1}\right] + 1.5\ln\left(\frac{T_{\mathrm{e}}}{\mathrm{K}}\right)\right\}. \tag{3}$$

T_{e} is the electron temperature given by Paladini et al. (2004) and Tibbs et al. (2012)

$$T_{\mathrm{e}} = (4166 \pm 124) + (314 \pm 20) \times d\ \mathrm{K}. \tag{4}$$

According to the rotation curve models of Fich et al. (1989), the Galactocentric distance d of H II regions can be given by

$$d = \frac{V - a_1 V_\odot}{a_2 \omega_\odot}, \tag{5}$$

where V is the rotation velocity of an H II region around the Galactic center at a Galactocentric distance, and $V_\odot$ and $\omega_\odot$ are the rotation velocity and angular velocity of the Sun. The fitting coefficients a_1, a_2 and $\omega_\odot$ are 0.99334, 0.0030385 and 27.5 km s^{-1} (Fich et al. 1989), respectively. In the survey of H II regions made with Arecibo, because they did not give the flux density of each H II region at 9 GHz, we replace the flux by that at 1.4 GHz. The obtained electron temperature, ionizing luminosity and age of 18 H II regions are listed in Table 2.

From Table 2, we see that T_{e} ranges from 5627 K to 6839 K in these H II regions, and the averaged T_{e} is 6083 K; $a(\nu, T_{\mathrm{e}})$ is about 0.9 for all the H II regions. Moreover, t_{HII} ranges from 3.0×10^5 yr to 1.7×10^6 yr, and the mean age is 7.7×10^5 yr.

3.2 CO Molecular Gas Associated with H II Regions

3.2.1 The morphology of the molecular clouds

To show the morphology of the molecular clouds associated with H II regions, we superimposed the velocity-integrated intensity maps of ^{13}CO(1–0) onto the map of each H II region. The velocity ranges are obtained from the spectrum marked by two vertical dashed lines in Figure 1 (left panels). In Figure 1 (right panels), each H II region may coincide with the surrounding molecular clouds. Based on the morphology of molecular clouds associated with an H II region, these H II regions are divided into three groups.

Table 2 Parameters Obtained for the H II Regions

No.	Region	d (kpc)	T_e (K)	$a\,(\nu, T_e)$	Q_{Ly} (photon s^{-1})	t_{HII} (yr)
1	G19.504–0.193	5.6	5935±237	0.9	(3.7±0.4)×10^{48}	(3.6±0.1)×10^{5}
2	G19.813+0.010	4.9	5694±221	0.9	(3.5±0.5)×10^{48}	(9.8±0.4)×10^{5}
3	G23.029–0.405	4.7	5627±217	0.9	(3.1±0.4)×10^{48}	(5.3±0.2)×10^{5}
4	G26.824+0.380	4.8	5673±220	0.9	(3.9±0.7)×10^{47}	(4.7±0.2)×10^{5}
5	G29.007+0.076	5.2	5802±228	0.9	(8.1±0.7)×10^{48}	(1.0±0.2)×10^{6}
6	G32.587+0.006	5.3	5834±230	0.9	(3.5±0.3)×10^{48}	(6.6±0.1)×10^{5}
7	G32.976–0.334	6.1	6079±246	0.9	(7.9±0.8)×10^{48}	(1.1±0.1)×10^{6}
8	G33.718–0.410	6.5	6079±246	0.9	(2.2±0.5)×10^{47}	(3.0±0.2)×10^{5}
9	G34.325+0.211	5.7	6211±254	0.9	(4.3±0.5)×10^{48}	(9.6±0.3)×10^{5}
10	G38.353–0.134	5.8	5958±238	0.9	(7.6±0.6)×10^{47}	(6.5±0.1)×10^{5}
11	G38.643–0.227	5.9	5997±241	0.9	(8.7±0.2)×10^{47}	(6.0±0.4)×10^{5}
12	G38.738–0.140	6.6	6004±241	0.9	(2.2±0.2)×10^{48}	(4.9±0.1)×10^{5}
13	G38.930–0.386	6.0	6240±256	0.9	(3.6±1.7)×10^{46}	(1.1±0.2)×10^{6}
14	G41.132–0.558	6.1	6055±244	0.9	(6.4±1.1)×10^{46}	(8.4±0.4)×10^{6}
15	G41.239–0.176	7.6	6076±246	0.9	(4.4±0.9)×10^{48}	(5.2±0.2)×10^{5}
16	G41.928+0.029	6.3	6551±276	0.9	(1.0±0.6)×10^{49}	(7.3±0.2)×10^{5}
17	G43.738+0.114	6.1	6082±246	0.9	(6.3±1.0)×10^{46}	(1.7±0.3)×10^{6}
18	G43.770+0.070	6.1	6031±243	0.9	(1.8±0.3)×10^{48}	(6.7±0.3)×10^{5}
19	G44.339–0.827	6.1	6090±247	0.9	(6.7±1.8)×10^{47}	(9.3±0.6)×10^{5}
20	G45.770–0.372	6.3	6138±250	0.9	(5.5±0.7)×10^{46}	(7.4±0.8)×10^{5}
21	G46.176+0.536	7.9	6642±282	0.9	(3.7±1.1)×10^{47}	(5.7±0.2)×10^{5}
22	G47.028+0.232	6.3	6155±251	0.9	(1.7±0.2)×10^{48}	(6.6±0.1)×10^{5}
23	G49.738–0.616	6.1	6090±247	0.9	(1.2±1.2)×10^{47}	(1.3±0.5)×10^{6}
24	G50.039–0.274	6.3	6144±250	0.9	—	—
25	G50.079+0.571	8.5	6839±294	0.9	(3.0±0.5)×10^{48}	(6.4±0.3)×10^{5}

(1) Those having compact molecular cores regularly spaced on the borders of the H II region traced by PAH emission, such as G19.504–0.193, G19.813+0.010, G23.029–0.405, G26.824+0.380, G32.587+0.006, G32.976–0.334, G33.718–0.410, G38.643–0.227, G38.738–0.140, G38.930–0.380, G41.928+0.029, G43.738+0.114, G43.770+0.070, G46.176+0.536 and G50.039–0.274. Massive stars form in giant molecular clouds. When ultraviolet radiation from these stars produces H II regions, they may not be far away from their natal molecular clouds. With the expansion of the H II regions, some dense cores may form in a compressed layer of the molecular clouds between the ionization front and shock front that precedes it in the molecular clouds. Gradually, a dense core is retained in the compressed layer, but the low density regions of molecular clouds may be dispersed.

(2) Those that show some dense clumps that form between the H II regions and the surrounding giant molecular clouds, such as G29.007+0.076, G34.325+0.211, G38.353–0.134, G41.132–0.558, G41.239–0.176, G44.339–0.827, G45.770–0.372, G47.028+0.232 and G49.738–0.616. When massive stars form on or near borders of giant molecular clouds, the expansion of H II regions causes molecular gas between the giant molecular clouds and H II region to accumulate. Hence, some dense clumps form in the compressed layer.

(3) Those that have molecular clouds covering the entire H II region, such as G50.079+0.571. This case indicates that these H II regions are still embedded in the giant molecular clouds.
In H II regions G29.007+0.076, G44.339–0.827 and G47.028+0.232, the PAH emission all shows a cometary structure. Moreover, the whole filamentary molecular cloud that is interacting with the PAH emission of G47.028+0.232 exhibits a cometary structure. These three H II

regions support the RDI model. The other H II regions are classified into groups 1 or 2. These molecular clouds have a compact core that is regularly distributed around the PAH emission, which is strong evidence in favor of the CC model. In addition, with the evolution of the H II region, the H II regions in group 3 may assume the same morphology as those in groups 1 and 2.

3.2.2 The physical parameters of the molecular clouds

Assuming local thermodynamical equilibrium and using the ^{13}CO(1–0) line, the column density of the clumps in cm^{-2} was estimated to be (Garden et al. 1991)

$$N_{\mathrm{H_2}} = 1.25 \times 10^{15} \int T_{\mathrm{mb}} \mathrm{d}v \ \ \mathrm{cm}^{-2} \,, \qquad (6)$$

where $\mathrm{d}v$ is the range of velocity in km s^{-1}. Here we adopt a relation $N_{\mathrm{H_2}} \approx 5 \times 10^5 N_{^{13}\mathrm{CO}}$ (Simon et al. 2001) and the average excitation temperature of 20 K from previous studies (Paron et al. 2011; Dirienzo et al. 2012). If the clumps are approximately spherical in shape, the mean number density H$_2$ is $n(\mathrm{i}){=}1.62 \times 10^{-19} N_{\mathrm{H_2}}/L$, where L is the diameter of the clump in parsecs (pc). If the clump has an irregular shape, we use an effective radius, which is the radius of a circle that has the same solid angle on the sky as the clump. The derived column density of each clump is listed in Table 1, which ranges from $2.3{\times}10^{21}$ cm^{-2} to $7.3{\times}10^{22}$ cm^{-2}. These values are compatible with the theoretical predictions of Whitworth et al. (1994), who show that for a wide range of input parameters, the gravitational fragmentation of a shocked layer occurs when the column density of this layer reaches a value $\sim 6.0{\times}10^{21}$ cm^{-2}. In 25 H II regions, the derived column density of 21 H II regions is lower than the value of Whitworth et al. (1994), implying that the shocked layer of these H II regions has been gravitationally fragmented.

3.2.3 Outflow detected

Surveys of the Galactic plane using the continuum at millimeter wavelengths provide the most efficient way to find molecular clumps that are the likely formation sites of massive stars and star clusters. Using data from the Bolocam Galactic Plane Survey (BGPS), we selected the BGPS sources surrounding each H II region. From Figure 1 (right), we can see that there are several BGPS sources (green pluses) distributed along the bubble of each H II region, except for G41.132–0.558, G41.928+0.029, G43.738, G43.770, G44.339–0.827, G46.176+0.536, G49.738–0.616, G50.039–0.274 and G50.079+0.571. Furthermore, some BGPS sources are located at the center of molecular cores. An outflow is strong evidence of earlier star-forming activity. In order to search for signs of star-forming activity, we try to detect outflows from these BGPS sources that are associated with H II regions and molecular cores. If several cores are linked together, then it is difficult to determine the component of the outflows. Hence, we only selected the BGPS sources associated with isolated cores. In 25 H II regions, we find that the molecular cores associated with seven H II regions satisfy the above criterion. For these molecular cores, we first drew position-velocity (P-V) diagrams. Using the P-V diagrams, we selected the integrated range of wings and determined the outflow intensities of red and blue lobes. Seven molecular outflows were identified by the contours of integrated intensities of ^{13}CO(1–0) line wings in H II regions G19.504–0.193, G19.813+0.01, G23.029–0.405, G26.824+0.380 and G38.930+0.380, shown in Figure 2.

The dynamic timescale of each outflow is estimated by equation $t_{\mathrm{out}} = 9.78 \times 10^5 \mathrm{R/V}$ (yr), where V, in km s^{-1}, is the maximum velocity of the flow relative to the cloud's systemic velocity, and R, in pc, is the size of the outflow defined by the length of the extension of the flow for each blueshifted and redshifted lobe. The mean dynamic timescale of each outflow is listed in Table 3.
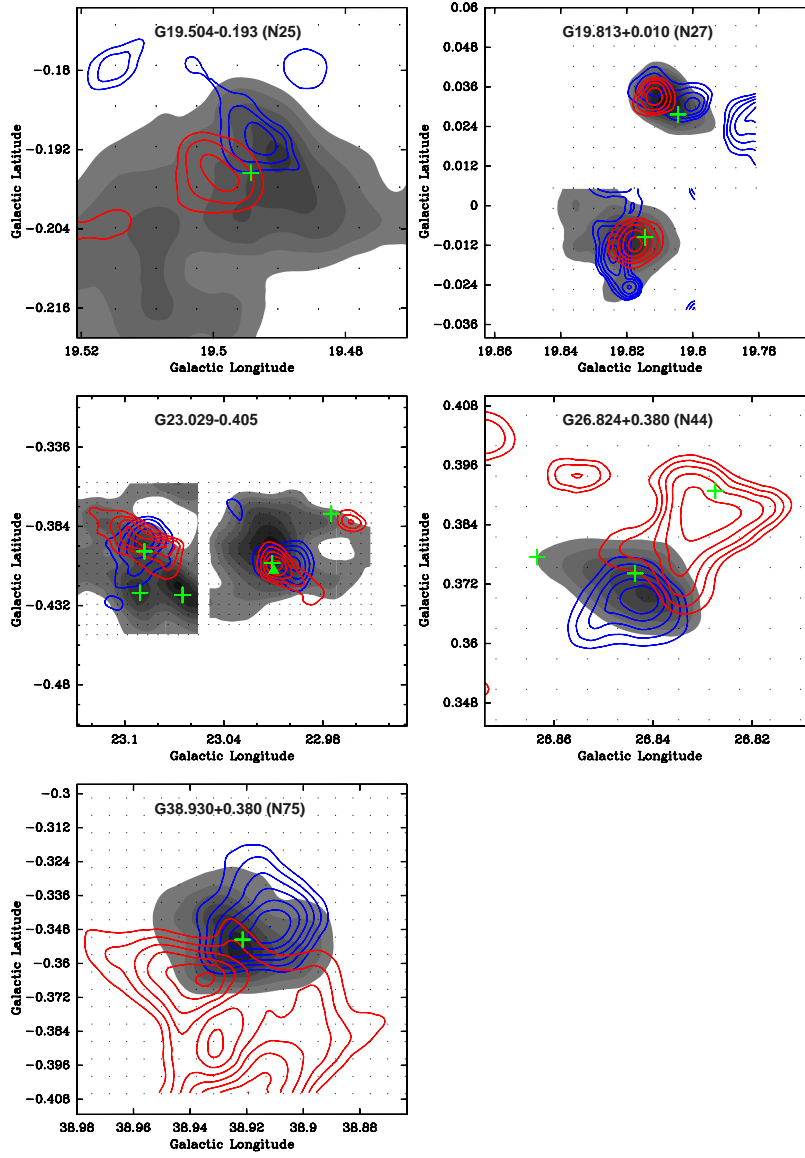
Fig. 2 The contour maps of outflows overlaid with the ^{13}CO(1–0) emission of each clump (gray scale). G19.504–0.193: The blue contour levels are 0.9, 1.0 and 1.1 km s^{-1}, while the red contour levels are 0.9, 1.0 and 1.1 km s^{-1}. G19.813+0.01: (*Top*) The blue contour levels are 0.5, 0.6, 0.7 and 0.8 km s^{-1}, while the red contour levels are 0.5, 0.6, 0.7 and 0.8 km s^{-1}. (*Bottom*) The blue contour levels are 0.2, 0.3, 0.4, 0.5 and 0.6 km s^{-1}, while the red contour levels are 0.9, 1.1, 1.2, 1.3 and 1.4 km s^{-1}. G23.029–0.405: (*Left*) The blue contour levels are 10.0, 10.7, 7.0, 8.0, 9.0 and 10.0 km s^{-1}, while the red contour levels are 5.0, 6.0, 7.0 and 8.0 km s^{-1}. (*Right*) The blue contour levels are 10.0, 10.7, 11.4, 12.1, 12.8, 13.6 and 14.3 km s^{-1}, while the red contour levels are 10.0, 10.7, 11.4, 12.1, 12.8, 13.6 and 14.3 km s^{-1}. G26.824+0.380: The blue contour levels are 0.5, 0.6, 0.7, 0.8 and 0.9 km s^{-1}, while the red contour levels are 0.4, 0.5, 0.6 and 0.7 km s^{-1}. G38.930+0.380: The blue contour levels are 2.4, 3.1, 3.8, 4.5, 5.2, 6.0 and 6.7 km s^{-1}, while the red contour levels are 1.8, 2.3, 2.8, 3.3, 3.8, 4.3 and 4.8 km s^{-1}.

Table 3 Parameters Obtained for the Outflow

No.	Region	BGPS	l (°)	b (°)	t_{out} (10^5 yr)
1	G19.504–0.193	G19.490–0.197	19.494	–0.196	2.7
2	G19.813+0.010	G19.818–0.009	19.814	–0.010	6.5
		G19.806+0.033	19.804	0.028	6.4
3	G23.029–0.405	G23.012–0.410	23.011	–0.406	2.0
		G23.090–0.394	23.088	–0.399	2.5
4	G26.824+0.380	G26.843+0.375	26.844	0.374	3.8
5	G38.930+0.380	G38.920–0.352	38.921	–0.352	5.1

4 DISCUSSION

4.1 Assessment of Triggered Star Formation

The IRAS Point Source Catalog has revealed a number of stellar objects which are younger than pre-main sequence stars (Beichman et al. 1986; Fukui et al. 1989). Hence, an IRAS point source is a good marker of the very early stages of star formation. In order to explore a causal relationship between the H II regions and star formation, we have searched for protostellar candidates in the IRAS Point Source Catalog that fulfill the following selection criteria (Jankes et al. 1992 & Xu et al. 2011): (1) $F_{100} \geq 20$ Jy, (2) $1.2 \leq F_{100}/F_{60} \leq 6.0$, (3) $F_{25} \leq F_{60}$ and (4) $R_{\mathrm{IRAS}} \leq 1.5\,R_{\mathrm{HII}}$, where F_{25}, F_{60} and F_{100} are the infrared fluxes at three IR bands (25, 60 and 100 μm), respectively. The first criterion only selects strong sources. The second and third discriminate against the cold IR point sources that are probably associated with cool stars, planetary nebulae and cirrus clumps, while the fourth guarantees that the search diameter (R_{IRAS}) includes the complete surface of H II regions. IRAS sources were found in a search circle within a radius of $1.5\,R_{\mathrm{HII}}$ centered on each H II region. In 19 H II regions, we find 23 young IRAS sources satisfying the above criteria. The name, coordinates and flux at 12, 25, 60 and 100 μm of these IRAS point sources are listed in Table 4. Infrared luminosity (Casoli et al. 1986) and dust temperature (Henning et al. 1990) are expressed respectively as,

$$L_{\mathrm{IR}} = (20.653 \times F_{12} + 7.538 \times F_{25} + 4.578 \times F_{60} + 1.762 \times F_{100}) \times D^2 \times 0.30, \qquad (7)$$

$$T_{\mathrm{d}} = \frac{96}{(3 + \beta)\ln(100/60) - \ln(F_{60}/F_{100})}, \qquad (8)$$

where D is the distance from the Sun in kpc. The emissivity index of a dust particle (β) is assumed to be 2. The calculated results are presented in Table 4. From Table 4, we can see that the infrared luminosity L_{IR} of each IRAS source is larger than $10^3 L_\odot$, which is associated with that of bubble N131 (Zhang et al. 2013). The IRAS sources associated with the BRCs have L_{IR} from ~10 to $10^3 L_\odot$ (Sugitani et al. 1991). In addition, Junkes et al. (1992) found 17 IRAS sources associated with SNR G54.4–0.3, and for 16 of these sources, L_{IR} is $\leq 10^3 L_\odot$. Similarly, the luminosity L_{IR} of all the IRAS sources surrounding SNR IC443 is $< 10^3 L_\odot$ (Xu et al. 2011). BRCs found in H II regions are potential sites of triggered star formation by an RDI process. We suggest that the process of star formation triggered by SNRs may be similar to RDI.

Figure 1 (right panels) also shows the spatial distribution of the selected IRAS sources in 17 H II regions. From Figure 1 (right panels), we see that all the IRAS sources are associated with PAH emission and some IRAS sources are located at the peak of ^{13}CO molecular clumps, indicating that these IRAS sources have larger infrared luminosity that may have been triggered by the CC process.

To further search for primary tracers of star-formation activity in the surroundings of H II regions, we used the GLIMPSE I catalog, which consists of point sources that are detected at least twice in one band. Based on the photometric criteria of Allen et al. (2004), we search for young

Table 4 Selected IR Point Sources Near 25 H II Regions: IR Flux Densities, Dust Temperatures and IR Luminosities.

No.	Source	l (°)	b (°)	F_{12} (Jy)	F_{25} (Jy)	F_{60} (Jy)	F_{100} (Jy)	T_d (K)	L_{IR} ($10^4 L_\odot$)
1	IRAS 18244–1201	19.524	–0.185	5.06	33.3	732.7	2011.0	26.9	35.7
2	–	–	–	–	–	–	–	–	–
3	IRAS 18317–0903	22.987	–0.381	4.8	45.1	1144.0	4999.0	23.8	9.6
	IRAS 18319–0903	23.012	–0.422	4.8	25.0	1144.0	4592.0	24.3	9.1
4	–	–	–	–	–	–	–	–	–
5	IRAS 18413–0331	28.995	0.082	4.8	14.3	335.1	577.5	31.0	11.0
6	IRAS 18482–0021	32.590	0.001	10.0	8.2	109.7	470.8	23.9	4.5
7	IRAS 18501–0009	32.998	–0.338	3.0	10.4	162.1	737.1	23.5	7.9
8	IRAS 18518+0026	33.716	–0.420	3.1	1.0	39.8	224.7	22.4	0.2
9	IRAS 18507+0118	34.362	0.206	2.5	12.1	765.4	1948.0	27.5	22.5
10	–	–	–	–	–	–	–	–	–
11	IRAS 19002+0454	38.645	–0.225	2.2	11.3	120.3	285.6	28.1	2.7
12	–	–	–	–	–	–	–	–	–
13	IRAS 19015+0503	38.933	–0.456	2.2	6.8	497.2	1156.0	28.2	14.6
14	IRAS 19060+0657	41.136	–0.553	3.2	2.8	55.1	141.8	27.4	0.7
15	–	–	–	–	–	–	–	–	–
16	IRAS 19054+0754	41.916	0.007	1.6	1.5	16.8	51.0	26.2	0.8
	IRAS 19054+0755	41.923	0.035	0.6	4.1	84.4	186.7	28.7	3.0
17	IRAS 19086+0935	43.762	0.108	2.1	1.5	73.8	356.7	2.3	1.1
18	IRAS 19088+0935	43.788	0.059	3.1	17.1	71.0	235.1	25.6	1.1
19	IRAS 19130+0940	44.356	–0.822	3.5	0.9	150.9	557.2	24.9	2.0
20	–	–	–	–	–	–	–	–	–
21	IRAS 19116+1156	46.195	0.539	7.1	6.6	110.2	391.7	25.1	4.9
	IRAS 19116+1157	46.213	0.548	3.9	3.2	388.3	1297.0	25.5	14.6
	IRAS 19116+1155	46.182	0.531	2.5	5.2	486.2	1454.0	26.3	17.1
22	IRAS 19143+1232	47.029	0.241	3.0	6.9	169.2	519.4	26.1	1.8
23	IRAS 19227+1431	49.746	–0.623	3.1	2.2	24.8	75.7	26.2	0.3
24	–	–	–	–	–	–	–	–	–
25	IRAS 19191+1522	50.075	–0.560	2.5	7.6	206.4	607.1	26.4	7.8

stellar object (YSO) candidates within a circle of >1.5 radius centered in each H II region. From the database, we constructed a $[5.8] - [8.0]$ versus $[3.6] - [4.5]$ color-color diagram for each H II region to identify Class I and Class II YSOs. Class I sources (10^5 yr) are protostars with circumstellar envelopes, while Class II sources (10^6 yr) are disk-dominated objects.

Figure 1 (right panels) shows the spatial distribution of both Class I and Class II sources. From Figure 1 (right panels), we note that some Class I sources are only asymmetrically distributed in H II region G29.007+0.076, G44.339–0.827 and G47.028+0.232, and are mostly concentrated in the interacting regions between these H II regions and the surrounding molecular clouds. In H II regions G29.007+0.076 and G47.028+0.232, the Class I sources in the interacting regions are close to the center of the H II regions compared to the Class II sources. The existence of Class I and Class II sources may also indicate star formation activity.

Comparing the age of each H II region with the characteristic star-formation timescales, we conclude that the three H II regions can trigger clustered star formation. In addition, we find that the PAH emission of the three H II regions is stronger close to the molecular clouds, and all show a cometary globule, suggesting these Class I and Class II sources may be triggered by the RDI process. In addition, for the first time, we detected seven molecular outflows in H II regions G19.504–0.193, G19.813+0.01, G23.029–0.405, G26.824+0.380 and G38.930+0.380. The mean dynamic timescale of each outflow is larger than the age of the corresponding H II regions. Hence, we conclude that these outflow sources may have been triggered by the corresponding H II regions, but observations at higher spatial resolution are needed to resolve the detailed kinematics of the outflows in these H II regions.

5 CONCLUSIONS

In this work, we have performed a detailed analysis of the environment of 25 H II regions with bubble morphologies in ^{13}CO(1–0) and infrared data. These H II regions at 8 µm show the morphology of complete or partial bubbles, indicating PAH emission is destroyed inside the ionized region. Each H II region may be associated with the surrounding molecular cloud. In 25 H II regions, the derived column density of 21 H II regions is larger than the value from Whitworth et al. (1994), implying that the shocked layer in these H II regions has been gravitationally fragmented. We derived that the electron temperature ranges from 5627 K to 6839 K in these H II regions, and the average electron temperature is 6083 K. Moreover, the age of all the H II regions is from 3.0×10^5 yr to 1.7×10^6 yr, and the mean age is 7.7×10^5 yr. We selected 23 young IRAS sources with larger IR luminosity ($>10^3 L_\odot$) in 19 H II regions, which may have been triggered by the CC process. In addition, some YSOs (including Class I sources) are concentrated around H II regions G29.007+0.076, G44.339–0.827 and G47.028+0.232, which appear to be sites of ongoing star formation. The PAH emission of the three H II regions all shows a cometary globule. Comparing the age of each H II region with the characteristic timescales for star formation, we conclude that the three H II regions can trigger clustered star formation by the RDI process. In addition, for the first time, we detected seven molecular outflows in the five H II regions. These outflow sources may be related to the corresponding H II regions.

References

Allen, L. E., Calvet, N., D'Alessio, P., et al. 2004, ApJS, 154, 363
Anderson, L. D., Bania, T. M., Balser, D. S., & Rood, R. T. 2011, ApJS, 194, 32
Bania, T. M., Anderson, L. D., Balser, D. S., & Rood, R. T. 2010, ApJ, 718, L106
Bania, T. M., Anderson, L. D., & Balser, D. S. 2012, ApJ, 759, 96
Beichman, C. A., Myers, P. C., Emerson, J. P., et al. 1986, ApJ, 307, 337
Casoli, F., Combes, F., Dupraz, C., Gerin, M., & Boulanger, F. 1986, A&A, 169, 281
Churchwell, E., Povich, M. S., Allen, D., et al. 2006, ApJ, 649, 759
Condon, J. J., Cotton, W. D., Greisen, E. W., et al. 1998, AJ, 115, 1693
Dale, J. E., Bonnell, I. A., & Whitworth, A. P. 2007, MNRAS, 375, 1291
Deharveng, L., Lefloch, B., Kurtz, S., et al. 2008, A&A, 482, 585
Dewangan, L. K., Ojha, D. K., Anandarao, B. G., Ghosh, S. K., & Chakraborti, S. 2012, ApJ, 756, 151
Dirienzo, W. J., Indebetouw, R., Brogan, C., et al. 2012, AJ, 144, 173
Dyson, J. E., & Williams, D. A. 1980, Physics of the Interstellar Medium, ed. Dyson, J. E. & Williams, D. A. (New York: Halsted Press)
Fazio, G. G., Hora, J. L., Allen, L. E., et al. 2004, ApJS, 154, 10
Fich, M., Blitz, L., & Stark, A. A. 1989, ApJ, 342, 272
Fukui, Y., Iwata, T., Mizuno, A., Ogawa, H., & Takaba, H. 1989, Nature, 342, 161
Garden, R. P., Hayashi, M., Hasegawa, T., Gatley, I., & Kaifu, N. 1991, ApJ, 374, 540
Henning, T., Pfau, W., & Altenhoff, W. J. 1990, A&A, 227, 542
Jackson, J. M., Rathborne, J. M., Shah, R. Y., et al. 2006, ApJS, 163, 145
Junkes, N., Fuerst, E., & Reich, W. 1992, A&A, 261, 289
Kolpak, M. A., Jackson, J. M., Bania, T. M., Clemens, D. P., & Dickey, J. M. 2003, ApJ, 582, 756
Kuchar, T. A., & Bania, T. M. 1994, ApJ, 436, 117
Mezger, P. G., & Henderson, A. P. 1967, ApJ, 147, 471
Mezger, P. G., Smith, L. F., & Churchwell, E. 1974, A&A, 32, 269
Paladini, R., Davies, R. D., & De Zotti, G. 2004, MNRAS, 347, 237

Paron, S., Ortega, M. E., Rubio, M., & Dubner, G. 2009, A&A, 498, 445

Paron, S., Petriella, A., & Ortega, M. E. 2011, A&A, 525, A132

Pomarès, M., Zavagno, A., Deharveng, L., et al. 2009, A&A, 494, 987

Reipurth, B. 1983, A&A, 117, 183

Sandford, M. T., II, Whitaker, R. W., & Klein, R. I. 1982, ApJ, 260, 183

Simon, R., Jackson, J. M., Clemens, D. P., Bania, T. M., & Heyer, M. H. 2001, ApJ, 551, 747

Su, Y., Chen, Y., Yang, J., et al. 2009, ApJ, 694, 376

Sugitani, K., Fukui, Y., & Ogura, K. 1991, ApJS, 77, 59

Tibbs, C. T., Paladini, R., Compiègne, M., et al. 2012, ApJ, 754, 94

Whitworth, A. P., Bhattal, A. S., Chapman, S. J., Disney, M. J., & Turner, J. A. 1994, MNRAS, 268, 291

Xu, J.-L., Wang, J.-J., & Miller, M. 2011, ApJ, 727, 81

Xu, J.-L., & Wang, J.-J. 2012, A&A, 543, A24

Zavagno, A., Deharveng, L., Comerón, F., et al. 2006, A&A, 446, 171

Zavagno, A., Anderson, L. D., Russeil, D., et al. 2010, A&A, 518, L101

Zhang, C.-P., Wang, J.-J., & Xu, J.-L. 2013, A&A, 550, A117

Zhou, X., Chen, Y., Su, Y., & Yang, J. 2009, ApJ, 691, 516

Zinnecker, H., & Yorke, H. W. 2007, ARA&A, 45, 481